Plasma dynamically induced frequency shifts in high-order harmonic generation in nitrogen

Brandi, F.; Giammanco, F.; Ubachs, W.M.G.

published in
Laser Physics
2008

DOI (link to publisher)
10.1134/S1054660X08050071

document version
Publisher's PDF, also known as Version of record

citation for published version (APA)
Brandi, F., Giammanco, F., & Ubachs, W. M. G. (2008). Plasma dynamically induced frequency shifts in high-order harmonic generation in nitrogen. *Laser Physics*, *18*(5), 585-591. https://doi.org/10.1134/S1054660X08050071

ISSN 1054-660X, Laser Physics, 2008, Vol. 18, No. 5, pp. 585–591.

Plasma Dynamically Induced Frequency Shifts in High-Order Harmonic Generation in Nitrogen

F. Brandi[a], F. Giammanco[a, *], and W. Ubachs[b]

[a] *Department of Physics, University of Pisa, Largo Bruno Pontecorvo 3, Pisa, 56127 Italy*
[b] *Laser Centre, Department of Physics and Astronomy, Vrije Universiteit, De Boelelaan 1081, 1081 HV Amsterdam, The Netherlands*
*e-mail: giamma@df.unipi.it

Received December 18, 2007

Abstract—Experiments and theoretical calculations on high-harmonic generation in nitrogen are presented in the regime of laser pulses of a 300-ps duration, where the plasma dynamics following the ionization of the medium plays a decisive role. The experiments are performed with ~4-GW Ti:sapphire laser pulses, giving rise to fully saturated ionization. The shifts between the exact harmonic frequency in the extreme ultraviolet and the integer multiple of the fundamental frequency are caused by the self-phase modulation of the laser pulse due to the time-dependent free-electron density in the plasma generated in the focal zone. Well-calibrated atomic resonances in the extreme ultraviolet measured through absorption in a secondary gas jet are used as frequency markers in the extreme ultraviolet for the accurate determination of the sign and magnitude of the frequency shifts. A theoretical model including both plasma dynamics and harmonic generation from atoms and ions has previously been developed, and successfully applied to explain the frequency red shift observed in xenon [Phys. Rev. Lett. **96**, 123904 (2006)]. The plasma-dynamical model is extended and applied to the results of the harmonic generation in nitrogen, fully explaining the observed harmonic frequency shifts in the 9th and 13th harmonic.

PACS numbers: 42.65.Ky, 52.35.Mw, 32.70.Jz

DOI: 10.1134/S1054660X08050071

1. INTRODUCTION

The measurement, control, and understanding of the frequency spectrum generated in the harmonic conversion of an intense laser source is a relevant issue in high-resolution spectroscopy. The spectral purity of the harmonics depends on the interplay of the frequency chirp of the fundamental pulse, the self-phase modulation of the fundamental pulse interacting with a nonlinear medium, and the intrinsic chirp of the harmonic generation (HG) process. In [1, 2], the results were presented on the 9th harmonic generation in the nonperturbative regime (or plateau regime) in Xe utilizing a 300 ps 4-GW tunable Ti:sapphire laser, based on seeding an amplifier chain with a narrowband CW laser beam, delivering nearly Fourier-transform limited pulses. The accurate frequency calibration of the generated harmonic was performed at the 10^{-7} precision level using well-calibrated atomic resonances as a frequency marker in the extreme ultraviolet. For this purpose, the absorption spectroscopy is performed under sub-Doppler conditions in a secondary Ar jet on the ($3p^6\,{}^1S_0 \longrightarrow 3p^5\,3d'[3/2]_1$) transition at $\nu_{Ar} = 3\,458\,611.8$ GHz, i.e., at 86.7 nm. The measured 9th harmonic central frequency is found to deviate from the expected integer multiple of the fundamental frequency. In usual applications of the nonlinear conversion with high intensity lasers in the femtosecond regime, a frequency blue shift is observed due to the increase of the free-electron density during multiphoton ionization [3, 4]. In the presently used regime of relatively long laser pulses (300 ps), harmonic red-shifts were also observed under certain conditions of gas density and laser intensity. In particular, in [2], the striking phenomenon of increasing red shifts was found as a function of increasing laser intensities, although only for certain gas densities; there also exist conditions for which blue shifts were observed. This somewhat unexpected behavior could be explained in a plasma-dynamical model involving HG in combination with the temporal and spatial evolution of the plasma generated in the laser focus by multiphoton ionization (MPI) [2]. A comparison with the model also provided firm evidence that HG is not only produced from neutrals, but also from ions in the focal zone.

According to [2], the onset of a red shift is due to the plasma expansion becoming effective immediately after the MPI process. The time scale of the plasma expansion depends on several parameters, such as the degree of ionization, the absolute gas density, and the ion mass. For the present conditions, this time scale is, however, longer than that of the MPI process for peak intensities higher than the saturation threshold. Therefore, the HG from neutrals is not affected by the red shift induced by the decrease of the electron density resulting from the plasma expansion. As a consequence, an additional mechanism of HG, which becomes effective when the medium is fully ionized,

must be introduced to account for the observed net red shift for selected experimental parameters. To explain the results in Xe, we included the contribution to the HG from the bounded electrons of the ion in the soft-core potential model [2]. The HG from ions has already been predicted to be of comparable efficiency with that from the neutrals [5–7], although without providing direct experimental evidence of a large relative contribution of the ions compared with the neutrals. Moreover, a strong correlation between the harmonic and ion signals was observed in a typical experiment of the HG in the picosecond regime [8]. Based on these findings, it was hypothesized that a relevant contribution to the HG should be ascribed to the ionized medium for tens of picosecond laser pulses. The HG was initially ascribed to a mechanism based on a stimulated bremsstrahlung (SB) due to the free-electron scattering in the ion potential [9, 10]. Since the basic features, including the spectral response of the SB, were similar to those of the HG from the bound electrons, the SB was then assumed to be the dominant mechanism for describing the harmonic conversion in a fully ionized medium.

As pointed out in [2], the analysis of the frequency shift leads to new insights on the HG in the picosecond regime and to definitely abandon the SB scheme. In fact, the observed net shifts result from the occurrence of several phenomena during the laser pulse. First, the harmonics generated by the neutrals undergo a net blue shift due to the ionization of the neutrals and the creation of free electrons, thereby increasing the index of refraction. Second, a red shift occurs after the medium is fully ionized due to the plasma expansion and the fly-out of some electrons. Hence, in order to obtain a net red shift under certain conditions, the efficiency of the HG for the ionized medium must be comparable with that from the neutrals, whereas the SB is largely less efficient than the HG from the parent ions. In the following, we give an outline of the theoretical model used to describe the frequency-shift phenomena and compare the theoretical curves with the experimental results in N_2. The analysis of the dependences of the frequency shift on the experimental parameters yields new insights into the overall phenomenon. Moreover, we evaluate the influence on the net shift of the molecular dynamics, i.e., the direct and/or sequential dissociation.

2. EXPERIMENTAL SETUP

The experimental setup for the harmonic generation and the XUV frequency metrology methods have been described in previous papers [1, 2]. The laser system involves the amplification of a continuous wave (CW) Ti:sapphire beam in a sequence of three pulsed-dye amplifiers (PDA) and subsequent amplification in a Ti:sapphire multipass bowtie amplifier. The continuous tuning of the harmonic frequency is achieved by scanning the CW-laser frequency [11]. The PDA is pumped by the green output of a Nd:YAG laser (532 nm) after compressing the pulses to a 300-ps duration in a Brillouin cell filled with clean water [12]. In view of the fast response of the infrared dyes, the temporal profile of the laser pulses produced in the PDA follow those of the pump (300 ps), and have a nearly Fourier-limited bandwidth of about 1.5 GHz. The amplification in the Ti:sapphire bowtie retains the pulse duration and bandwidth produced in the PDA. The maximum energy of the laser system is 300 mJ in 300 ps with a diameter of 0.6 cm.

The harmonics are generated by focusing the laser beam by a 15-cm focal length lens, achieving intensities of up to 5×10^{13} W/cm^2, in a freely expanding gas jet at about 0.5 mm downstream from the 1-mm orifice of a pulsed valve. The interaction length is about 1 mm. The backing pressure and the pressure in the chamber were found to be linearly correlated [13]. An estimation of the gas density in the interaction region, based on the valve aperture time and orifice and the geometry of the chamber, yields another proportionality relation with the backing pressure, i.e., 1-bar backing corresponding to a density of 5×10^{17} atoms/cm^3 in the interaction region. Although rough, this value constitutes a reference for the density scale used in the numerical calculations (see below). The harmonics are dispersed by a spectrometer equipped with a gold-coated normal incidence grating and detected by an electron-multiplier tube. To analyze the spectral features, the harmonic selected by the spectrometer is then fed into a chamber, where an absorption experiment is performed in a secondary free jet produced by a synchronized pulsed valve injecting the absorbing medium. In particular, to measure the central frequency of the 9th harmonic, we use the well-calibrated transition in Ar, i.e., $3p^6\ {}^1S_0 \longrightarrow 3p^5 3d'[3/2]_1$, at the frequency $\nu_{Ar} = 3\,458\,611.8$ GHz, or roughly 86.7 nm. To measure the frequency of 13th harmonic, we use the He $1s4p$ resonance line at 52.2 nm [11].

Finally, the fundamental frequency (of the CW-seed laser) was measured by an ATOS (model LM-007) wavelength meter. In a PDA, chirp occurs due to the time-dependent gain in the dye-amplifier chain [14], inducing a net shift between the central frequency of the pulsed laser and the CW-seed frequency. That shift was carefully measured from the transmission profile through an etalon at different wavelengths on both sides of the gain curve. In particular, for the wavelengths of interest in the present study, the PDA-induced chirp for the 9th harmonic equals –2 GHz at 780 nm and +2 GHz at 750 nm. In the following, the blue- and red-shift phenomena related to the plasma dynamics in the harmonic conversion processes are corrected for this chirp phenomenon at the fundamental laser frequency.

3. THEORETICAL MODEL

We use the two-fluid approach to describe the dynamics of the plasma in the interaction region [10,

15]. The constitutive fluid system includes two continuity equations, two equations of motion, and two equations for the electron and ion temperatures. The continuity equations contain as a source term the ionization rate, where the probability of the MPI is expressed in terms of the saturation intensity as in [16]. We found that the calculated value is in fair agreement with our measurement on the saturation intensity [1, 2]. The equations for the electron and ion motion are coupled by the self-generated electric field and, for the electrons, by the momentum-exchanging electron-ion collisions. To introduce a simplification in the numerical integration, we consider only the radial component of the electric field, which is calculated by the direct integration of the Maxwell equation for $\nabla \cdot \mathbf{E}$ in a cylindrical symmetry [2], i.e.,

$$E_\rho(r, z, t) = \frac{e}{\varepsilon_0 r}\int_0^r [N_i(r, z, t) - N_e(r, z, t)] r dr. \quad (1)$$

The equation for the electron temperature includes heating via inverse bremsstrahlung and via the thermal exchange with ions, while the equation for the ion temperature involves only the latter of the two. Actually, the ion heating will turn out to be negligible during the laser pulse under our experimental conditions; this provides further proof that the ion expansion is driven by the Coulomb repulsion.

Before displaying the full set of equations, it is worthwhile to discuss the approximations that will be introduced to simplify the numerical integration. Owing to the gas density range of the experiment, i.e., 10^{17}–10^{-18} atoms/cm^3, the self-generated electric field plays a crucial role. Since the electrons move rapidly away from the interaction volume as they are produced, a dynamic charge imbalance occurs during the MPI process generating a large local electric field. The electric field competes with the electron expansion, which depends on the electron temperature and on the electron-density gradient. In particular, the time scale of the thermal expansion is given by $\tau_{\text{the}} = \frac{d}{V_{\text{the}}}$, where d is the size of the electron distribution and V_{the} is the thermal velocity. With $T_e = 1$ eV, i.e., the typical value of the residual kinetic energy of the MPI, $kT_e = nh\nu - I_p$, and $d_r = 15$ μm is the radial spot size, we find $\tau_{\text{the}} = 26$ ps, a value comparable with the time scale of the growth of the ionization. In addition, the electron temperature increases to tens of electronvolts due to the inverse bremsstrahlung absorption, thus leading to a further enhancement of the thermal velocity. Note that the time scale of the thermal expansion justifies the assumption of radial symmetry of the electric field. In fact, the length of the interaction zone, i.e., about 0.1 cm, is much greater than its radial size. It turns out that the charge imbalance is mainly due to the radial expansion of electrons.

The spatial scale that accounts for the balance between the electric field and the electron thermal expansion is given by the Debye length [15], i.e., $\lambda_D = \left(\frac{\varepsilon_0 kT_e}{e^2 N_i}\right)^{1/2}$ m. In our density range, λ_D becomes much shorter than d_r immediately after the onset of the MPI process on the order of about 10^{-6} cm. λ_D together with the electron plasma frequency, $\omega_{pe} = \left(\frac{e^2 N_e}{\varepsilon_0 m}\right)^{1/2} \approx 5.5 \times 10^{13}$ rad/s with $N_e = 10^{18}$ electrons/cm^3, define the spatial and temporal steps for the numerical integration of the fluid system. By combining these parameters, we find that the numerical integration of the continuity and velocity equations for the electrons would require a time step of less than $\leq 10^{-20}$ s for a charge density of 10^{18} charges/cm^3 to prevent numerical instabilities. This would take a very long integration time for any set of the initial parameters.

To simplify the numerical problem, we choose a spatial integration step sufficiently small to provide spatial details about the ion motion and the harmonic generation regardless of the local value of the Debye length. As a consequence, we consider the local behavior of electrons in each spatial cell, neglecting the nonlinear term $\mathbf{V}\nabla\mathbf{V}$ in the equation for the electron motion and limiting the excursion of the electron density around the ion density into a range defined by λ_D (see below). We assume a cylindrical geometry, so that all quantities are functions of r, z, and t.

The basic set of equations for the fluid model to calculate the spatiotemporal evolution of electrons and ions is then [15]

Continuity:

$$\frac{\partial N_j}{\partial t} + \nabla(N_j V_j) = S_j, \quad j = i, e. \quad (2)$$

Ion motion:

$$\frac{\partial \mathbf{V}_i}{\partial t} + \mathbf{V}_i \nabla \mathbf{V}_i = \frac{e\mathbf{E}}{M} - \frac{\nabla N_i kT_i}{MN_i} - \mathbf{V}_i \frac{S_i}{N_i}. \quad (3)$$

Electron motion:

$$\frac{\partial \mathbf{V}_e}{\partial t} = -\frac{e\mathbf{E}}{m} - \frac{\nabla N_e kT_e}{mN_e} - \nu_{ei}\mathbf{V}_e - \mathbf{V}_e \frac{S_e}{N_e}. \quad (4)$$

Electron temperature:

$$\frac{\partial kT_e}{\partial t} = 2\nu_{ei}U_p - \frac{m}{M}\nu_{ei}(kT_e - kT_i). \quad (5)$$

Ion temperature:

$$\frac{\partial kT_i}{\partial t} = \frac{m}{M}\nu_{ei}(kT_e - kT_i), \quad (6)$$

where S_j represents the source term of the ionization. Since collision processes such as recombination and

impact ionization are negligible, the growth of the ionization depends only on the MPI. Then, the rate equation can be written in the integral form, i.e., $N_R = N_G(1 - \exp[-\beta P_0^n \int_0^t f^n(t)dt])$, where N_R and N_G represent the charge and gas densities, respectively. The laser intensity is given by $P_0(r, z, t)f(t)$, where P_0 is the peak intensity, and n and β are the order and the probability of the MPI process, respectively. In particular, by assuming a Gaussian-shaped (temporal) laser pulse, we relate β to the intensity of saturation P_{sat}, namely, $\beta = \left(\frac{n}{\pi}\right)^{1/2} \frac{1}{\tau_L P_{sat}^n}$. Finally, we express the source term as $S_{i,e} = \frac{\partial N_R}{\partial t}$. P_{sat} is calculated by the formula of [16] for the MPI.

The electron-ion collision frequency in a singly ionized thermal plasma is given by [9]

$$\nu_{ei} = \left(\frac{2}{m}\right)^{1/2} \frac{e^4 N_e}{kT_{eff}^{3/2}} \ln\Lambda, \tag{7}$$

where $\ln\Lambda$ is the Coulomb logarithm $\Lambda = 1.5\frac{(kT_{eff})^{3/2}}{(4\pi)^{1/2} e^3 N_e^{1/2}}$.

U_p is the ponderomotive potential, $U_p = \frac{1}{4}\frac{e^2 E_L^2}{m\omega^2}$, while E_L and ω are the laser field intensity and frequency, respectively. T_{eff} in Eq. (7) is given by $kT_{eff} = kT_e + U_p$ to account for the overall kinetic energy of electrons, when U_p becomes greater than T_e [9]. The first right-hand term of Eq. (5) represents the inverse-bremsstrahlung absorption under the condition $\nu_{ei} \ll \omega$, which is fulfilled well in our experiment.

To control the numerical integration, we introduce an upper and lower limit for the electron density in each radial cell. In particular, we set the upper limit of $N_e(r, z, t)$ equal to the local value of ion density $N_i(r, z, t)$. To calculate the lower limit $N_{e\min}$, we assume that the maximum radial excursion of electrons is given by $d_e = d_r + \lambda_D$ and, hence, $N_{e\min} = N_i\left(\frac{d_r}{d_r + \lambda_D}\right)^2$. Therefore, the maximum charge separation ΔN is given by

$$\Delta N = N_i \frac{\lambda_D}{d_r}\left[\frac{2 + \lambda_D/d_r}{(1 + \lambda_D/d_r)^2}\right]. \tag{8}$$

Equation (8) limits the excursion of the electron density around the ion density and, hence, it will lead to an underestimation of the red shift. In fact, it reduces the effective positive field, at least, for some time after the onset of the ionization that drives the Coulomb repulsion.

The set of equations describing the plasma dynamics must be completed with a model to describe the harmonic generation and propagation. According to [2], the time evolution of the harmonic field required to calculate the net shift is calculated from the motion of a bound electron in a 1D Coulomb potential:

$$\frac{dV_e}{dt} = -\frac{eE_L}{m} - \frac{e^2}{m}\frac{X_{NL}}{(a^2 + X_{NL}^2)^{3/2}}, \tag{9}$$

where $X_{NL} = \frac{eE_L}{m\omega^2}\cos\omega t$ is the coordinate of the electron in the external laser field, with a the radius of the selected species, i.e., the neutral atom (molecule) or parent ion. According to [2], the frequency component of the qth harmonic is calculated at each r and z by the Fourier transform of the second right-hand term of Eq. (9) within an appropriate spectral width related to the laser pulse duration. Then, we evaluate the inverse Fourier transform entering the propagation equation. We subsequently obtain the radial profile of the qth harmonic output at each time step t after integration of the propagation equation along z. Finally, we compute the frequency shift by the weighted average of the instantaneous qth harmonic shift according to the following equation [2]:

$$\Delta\nu_q = q\frac{\int_0^{TR}\int_0^{TR} I_q(r, t)\Delta\nu_0(r, t)rdr}{\int_0^{TR}\int_0^{TR} I_q(r, t)rdr}, \tag{10}$$

where $\Delta\nu_0(r, t) = -\nu(L/c)\frac{\partial n_e(r, t)}{\partial t}$ is the instantaneous chirp of the fundamental frequency, n_e is the index of refraction of the electrons, and the instantaneous shift of the qth harmonic is simply q times $\Delta\nu_0(r, t)$. We have chosen the weighted average instead of the approach of calculating the shift directly from the Fourier transform. This approach has been found to be more convenient to speed up the numerical calculations especially at large densities, where the instantaneous shift undergoes very large excursions. Tests at low densities show a substantial equivalence between both methods. In the following section, we compare the numerical results with the observed dependences in N_2 on the gas density and laser intensity.

4. RESULTS AND DISCUSSION

Calculations in N_2 are complicated by the interplay of the multiphoton molecular dissociation and ionization and, eventually, the ionization of neutral N-atomic fragments, which affect both the harmonic generation and the effective charge density, i.e., the plasma dynam-

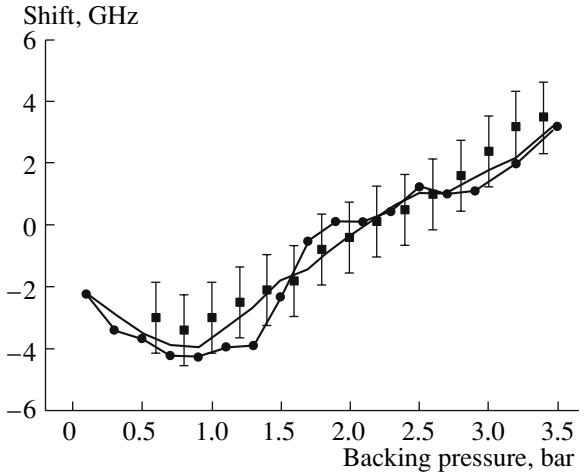

Fig. 1. Plasma dynamically induced shift of the 9th harmonic versus the molecular density at a power density of 4.5×10^{13} W/cm^2 in the focus. The horizontal scale, given in terms of the backing pressure to the pulsed valve, is proportional and can be converted to the gas density in the focus (see text). The laser wavelength is 780 nm. Data are corrected for the negative bias due to the chirp at the fundamental wavelength –2 GHz. Experimental data: solid square, N_2. Theoretical curves: solid thick line, N_2, $M = 14$; solid thick line with circles, N_2, $M = 28$.

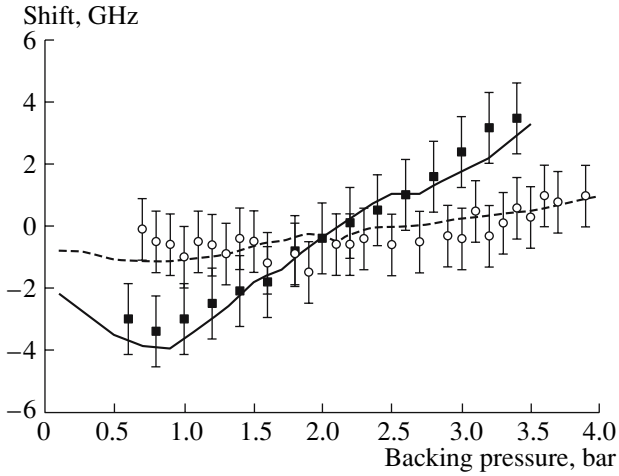

Fig. 2. Shift of the 9th harmonic in N_2 versus the backing pressure at $I = 4.5 \times 10^{13}$ W/cm^2 for two laser wavelengths λ_f = 751 and 780 nm. Experimental data: solid square, 780 nm with a bias of –2 GHz; open circles, 751 nm with a bias of +2 GHz. Theoretical curves: solid thick line, 780 nm; dashed thin line, 751 nm.

ics. Since the model for the harmonic generation given by Eq. (9) is only weakly affected by the choice of radius a of the emitter, the above processes primarily affect the plasma dynamics. To simplify the problem, we calculate the theoretical curves in two cases: first, by assuming N_2 is the neutral emitter and N_2^+ is the ion, while, in the second, molecular nitrogen is dissociated and N and N^+ are considered in the HG and the plasma dynamics. Hence, we compare the results with the experimental data to select the more appropriate description. Since we do not have a precise measure of the charge density, the calculations are performed over a wide density range. Thus, consistency can be found with the estimated neutral density in the jet, which, in the experiment, is correlated to the reading of the backing pressure before the expansion. It turns out that we cannot use the density/pressure scale to discriminate between processes, where either molecules or atomic fragments dominate the behavior. At best, we can only compare the deduced charge density in nitrogen with that found out in Xe [2].

Figure 1 shows the experimental results and theoretical calculations of the plasma dynamically induced frequency shift on the 9th harmonic in nitrogen. The curves were matched on a horizontal scale to fit the measured backing pressures with an optimum at 1 bar corresponding to the gas densities of 10^{18} neutrals/cm^3 used in the calculations. In [2] for Xe, a backing pressure of 1 bar was found to correspond to a density of 3×10^{17} atoms/cm^3 in the interaction region. These results do not allow us to distinguish the possible influence of N_2 dissociation, since the calculated curves for molecular and atomic nitrogen are rather close to each other, and within the experimental confidence limits.

Figure 2 shows the harmonic frequency shift versus the backing pressure for N_2 at two different laser wavelengths, i.e., 780 and 751 nm. The peak laser intensity is 4.5×10^{13} W/cm^2, which is above the saturation threshold of ionization, which is about 2.5×10^{13} W/cm^2. The selected wavelengths lie on the opposite side of the top of the gain curve of the PDA. The theoretical curves of Fig. 2 are corrected by the appropriate value of the bias related to the chirp effect in the PDA (see Section 2 and [2]). Figure 2 shows the striking features which highlight the role of the plasma dynamics. The behavior at 780 nm exhibits substantial differences compared with that at 750 nm. In fact, while below a backing pressure of about 1 bar the measured shift is nearly equal (apart from the difference bias), the shift at 780 nm increases much faster as the pressure increases. Neglecting the plasma dynamics, there is no way to explain this behavior, since the variation of the wavelength-dependent quantities, such as phase matching and HG, is too small within this range of wavelength variation. On the contrary, in the framework of the plasma dynamics, an explanation can be found in terms of an increase in the initial kinetic energy of the electrons. In fact, we find, following $kT_e = nh\nu - I_p$, kinetic energies of T_e (780) = 0.40 eV and T_e (750) = 0.95 eV. According to Eq. (8), a higher initial electronic kinetic energy enhances the charge separation and, hence, the plasma expansion. Although the red shift would be enhanced by a faster plasma expansion, the quadratic dependence of the HG intensity on the ion

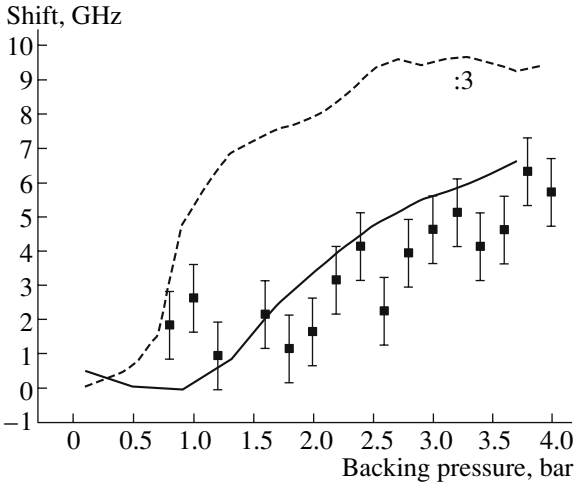

Fig. 3. Plasma dynamically induced shift of the 13th harmonic versus the backing pressure at 4.5×10^{13} W/cm^2 in N_2. The laser wavelength is 759 nm. Solid square dots, experiment; thick line, theory with a bias of +2 GHz; dashed line, calculated shift without plasma dynamics. The values of the dashed line are divided by a factor of three to better display the curves on the same scale.

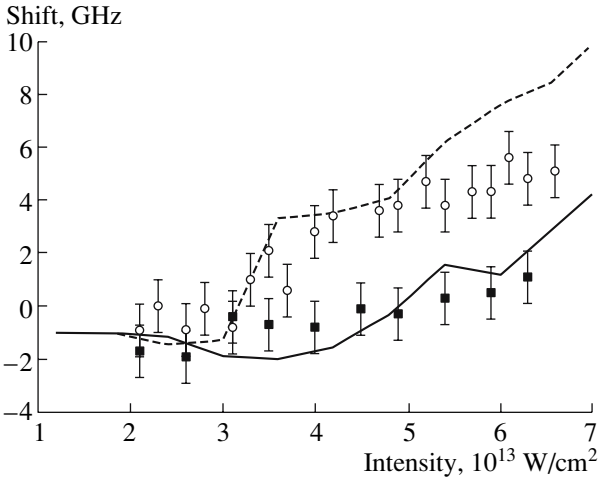

Fig. 4. Shift of the 9th harmonic versus the laser intensity in N_2. Solid square dots, experimental data at 1.4 bar of backing pressure; thick line, theoretical curve calculated for 1.4×10^{18} neutrals/cm^3 with a bias of –2 GHz; open circles, experimental data at 3.8 bar of backing pressure; dashed line, theoretical curve calculated for 3.8×10^{18} neutrals/cm^3.

density, which decreases faster as well, leads to a reduced weight of the red-shift contribution at 750 nm. As the density increases, the red shift increases as the square root of the charge density [2], while the blue shift is linearly dependent. Hence, the blue shift prevails more at 780 nm than at 750 nm. This explanation is confirmed by comparing the shift measured in Xe and N_2 under the same conditions [1]. According to the data reported in [1], Xe exhibits larger shifts than N_2 both red and blue in the same range of gas densities. Since the plasma expansion slows down more rapidly in Xe due to the higher mass, the contribution of the HG from the ions, which can undergo a red shift, is enhanced. To fully explain why the red shift (at a low-gas density) and the blue shift (at a high-gas density) is significantly higher in Xe than in N_2, the very different ionization thresholds should be taken into account. In fact, Xe is ionized in an early stage of the rising edge of the laser pulse, and, hence, the main contribution to the HG comes from the ions [2]. On the contrary, in N_2, the complete ionization occurs close to the peak intensity and, hence, it enhances the HG contribution from the neutrals, undergoing only a blue shift.

Figure 3 shows the dependence on the gas pressure of the 13th harmonic in N_2 at 4.5×10^{13} W/cm^2. Theoretical data are corrected on the bias of +2.8 GHz obtained by a linear rescaling of the 9th harmonic bias at 750 nm. These data provide us with further proof of the above picture. In fact, only a blue shift is obtained, since the 13th harmonic is generated within a narrow time interval around the peak intensity, where the plasma expansion is less effective. Nevertheless, the measured shift is far away from the values calculated excluding the plasma dynamics, as is shown by the dashed curve in Fig. 3. The deviation between the two calculations indicates the occurrence of a competing red shift. Therefore, it is not surprising that the results for the observed frequency shifts are not proportional to the harmonic order as we can verify by comparing curves of the 9th and 13th harmonics at 750 nm (see Fig. 2). In fact, the 9th harmonic is more influenced by the red shift due to the Coulomb expansion occurring after the MPI. On the other hand, if we calculate the shift neglecting the plasma dynamics, we obtain a linear dependence of the shift versus the harmonic order only at backing pressures below 1 bar. At higher pressures, the shift is strongly influenced by the phase-matching effects. Incidentally, it is worth noting that the role of the phase matching on the harmonic generation by the neutrals and ions is substantially modified by the plasma dynamics. In general, due to the plasma expansion, it becomes much less effective than what is expected by assuming a constant charge density after the MPI.

Figure 4 shows the dependence of the shift versus the laser intensity for two values of backing pressure, i.e., 1.4 and 3.8 bar and $M = 28$. The calculations assuming fully dissociated nitrogen, i.e., $M = 14$, are essentially coincident and not shown for the sake of clarity. The densities used to calculate the theoretical curves are 1.4×10^{18} and 3.8×10^{18} neutrals/cm^3 according to the normalization suggested previously. In nitrogen, we do not observe the striking dependence measured in Xe at 0.4 bar, i.e., a continuous increase in the red shift as the intensity increases [2]. Nevertheless, the red- and blue-shifting trends do exhibit similarities:

again, at the highest gas density, the largest blue shift is obtained.

5. CONCLUSIONS

We have demonstrated that the model, previously developed to explain plasma dynamically induced frequency shifts in Xe, can also explain the experimental data in N_2. In particular, this model presents an ab initio description of the phenomenon of the frequency shifts in the harmonic conversion, including the dependence on the experimental parameters such as laser pulse duration, peak intensity, and spot size, as well as on the specific atomic features such as the ionization potential, mass, and atomic/ionic radius. Although a full analysis can only be performed numerically, the model allows us to disentangle the role of different basic phenomena concurring to determine the measured shift, e.g., MPI, phase matching, and the HG from the neutrals and ions, electrons, and ion dynamics. Of course, the model is suited to describing the HG on time scales, where the plasma dynamics can occur, hence, for laser pulses exceeding some tens of picoseconds. At the same time, the model may be applicable to a wider class of laser-plasma interactions.

To conclude, we stress that new insight on the HG was uncovered thanks to a precise metrology on the fundamental laser frequency as well as on the harmonic frequency, which makes it possible to reach accuracies of 10^{-6}–10^{-7}. In particular, measurements of the shift dependencies in Xe versus the laser intensity, reported in [2], gave the main input to build a comprehensive model.

ACKNOWLEDGMENTS

This study was supported by the EC Integrated Infrastructure Initiative Action (RI3-CT-2003-506350) Project LCVU-1094.

REFERENCES

1. F. Giammanco, A. Pirri, F. Brandi, et al., Laser Phys. **15**, 328 (2005).
2. F. Brandi, F. Giammanco, and W. Ubachs, Phys. Rev. Lett. **96**, 123904 (2006).
3. J. J. Macklin, J. D. Kmetec, and C. L. Gordon III, Phys. Rev. Lett. **70**, 766 (1993).
4. C.-G. Wahlström, J. Larsson, A. Persson, et al., Phys. Rev. A **48**, 4709 (1993).
5. J. L. Krause, K. J. Schafer, and K. C. Kulander, Phys. Rev. Lett. **68**, 3535 (1992).
6. S. Kubodera, Y. Nagata, Y. Akiyama, et al., Phys. Rev. A **48**, 4576 (1993).
7. J. B. Watson, A. Sampera, and K. Burnett, Phys. Rev. A **51**, 1458 (1995).
8. F. Giammanco, P. Ceccherini, and T. Di Palma, Laser Phys. **11**, 368 (2001).
9. V. P. Silin, Quantum Electron. **29**, 11 (1999).
10. F. Giammanco, Phys. Rev. A **43**, 6939 (1991).
11. F. Brandi, D. Neshev, and W. Ubachs, Phys. Rev. Lett. **91**, 163901 (2003).
12. F. Brandi, I. Velchev, D. Neshev, et al., Rev. Sci. Instrum. **74**, 32 (2003).
13. D. Proch and T. Trickl, Rev. Sci. Instrum. **60**, 713 (1988).
14. S. Gangopadhyay, N. Melicheki, and E. E. Eyler, J. Opt. Soc. Am. B **11**, 231 (1994).
15. R. J. Goldston and P. H. Rutherford, *Introduction to Plasma Physics* (IOP Publishing, London, 1995).
16. B. Chang, P. R. Bolton, and D. N. Fittinghoff, Phys. Rev. A **47**, 4193 (1993).